"The Nature of Global Large-Scale Sea Level Variability
in Relation to Atmospheric Forcing: A Modeling Study"

by

chi e Fukumori

Ramanujan Raghunath

Lee-Lueng Fu

Jet Propulsion Laboratory, Mail Stop 300-323,
California Institute of Technology,
4800 Oak Grove Drive, Pasadena CA 91109
e-mail: if@pacific.jpl.nasa.gov

October 1, 1996

submitted for publication)

Abstract

The relation between large-scale sea level variability and ocean circulation is studied using a numerical model. A global primitive equation model of the ocean is forced by daily winds and climatological heat fluxes corresponding to the period from January 1992 to February 1996. The physical nature of the temporal variability from periods of days to a year, are examined based on spectral analyses of model results and comparisons with satellite altimetry and tide gauge measurements. The study elucidates and diagnoses the inhomogeneous dynamics of sea level variability in space and frequency domain. At mid-latitudes, large-scale sea level variability is primarily due to steric changes associated with the seasonal heating and cooling cycle. In comparison, changes in the tropics and high latitudes are mainly wind-driven. Wind-driven variability exhibits a strong latitudinal dependence in itself. Wind-driven changes are largely baroclinic in the tropics but barotropic at higher latitudes. Baroclinic changes are dominated by the annual harmonic of the first baroclinic mode and is largest off the Equator; Variabilities associated with equatorial waves are relatively small in comparison. Wind driven barotropic changes exhibit a notable enhancement over several abyssal plains in the Southern Ocean, which is likely due to resonant planetary wave modes in basins semi-enclosed by discontinuities in potential vorticity. Otherwise, barotropic sea level changes are typically dominated by high frequencies with as much as half the total variance in periods shorter than 20 days, reflecting the frequency spectra of wind-stress curl. Implications of the findings with regards to analyzing observations and data assimilation are discussed.

1

1. Introduction

Realistic numerical simulations of the ocean are now commonplace, in which model domain (i.e., topography and coast lines) and forcings are made compatible with (but not necessarily equal to) reality. Such simulations are useful in dynamically interpreting observations, and in making inferences of the important physical processes. More recently, such models are employed in synthesizing data, i.e., data assimilation. Data assimilation is an emerging area of oceanographic research in which models are used to interpolate and extrapolate observations (e.g., Ghil and Malanotte-Rizzoli, 1993). Of particular interest in assimilation is satellite altimetry measurements. The focus on altimetric assimilation stems from the fact that it is a time-continuous global observing system. Yet, some of the peculiarities of altimetric measurements have contributed to the difficulty of its exploitation. These include its complex sampling pattern according to satellite orbital dynamics and the fact that it is a measurement of sea level and not circulation per se, and which, in many large-scale primitive equation models, is a diagnostic quantity.

This study is motivated in part by use of numerical models in assimilating satellite altimetry data and examines the nature of large-scale temporal variability of the global ocean, with particular attention to sea level. Assimilation is in essence an inverse problem, and proper characterization of and insight into ocean physics can help facilitate the estimation process by aiding in the design of an effective assimilation scheme. We investigate the question of what underlying circulation large-scale sea level changes reflect. Based on a simple scaling argument, it can be shown that sea level to first approximation reflects circulation of the entire water column and not surface circulation alone (Pedlosky, 1987). For instance, Ezer and Mellor (1994) and Oschlies and Willebrand (1996) have demonstrated effective assimilation of altimetry data in the Gulf Stream region by assuming that sea level variabilities reflect changes in subsurface stratification, in particular the movement of the thermocline. In comparison, Gill and Niiler (1973) suggests that seasonal cycle of sea level at mid- to high- latitudes are due primarily to a local balance between near surface steric changes and surface heat flux. On the other hand, Chao and Fu (1995) found significant correlation between sea level and barotropic changes in circulation at high latitudes.

These past studies suggest sea level changes can be caused by different processes depending on latitude, regional dynamics (e.g., Gulf Stream), and time and spatial

2

scales. Most studies have examined the subject in limited geographic areas or frequency bands. The present study attempts a comprehensive re-examination of the dynamics of large-scale sea level variability uniformly over the global domain based on a numerical simulation. Due to computational limitations, the analysis is limited to scales larger than approximately 1000 km, and therefore the most energetic variabilities associated with meso-scale eddies are excluded from this investigation. A global coarse resolution primitive equation model is employed for this purpose forced by daily winds and climatological heat fluxes.

Past comparisons of numerical simulations with observations have established a zero-order similarity of such models and the ocean (e.g., Chao and Fu [1995], Stammer et al. [1996]). Yet, these studies also elucidate model shortcomings. For instance, the energy level of numerical models are still deficient especially at low frequencies. Therefore, caution should be exercised regarding reliability of such model simulations in general. Nevertheless, it is interesting to examine properties of numerical simulations, as it provides insight into salient physical processes of the ocean. At the least, it is important to understand the character of model physics in order to use them to analyze (i.e., assimilate) observations.

Characteristics of the model's temporal variability of sea level, velocity, and density are examined based on spectral analysis, and results are compared with measurements from TOPEX/POSEIDON and tide gauges to establish some measure of significance. Implications of the findings with regards to assimilating altimetric data will also be discussed, and the adequacy of the satellite's sampling characteristics addressed.

2. Model

The model used in this study is the Modular Ocean Model version 1.0 developed by the Geophysical Fluid Dynamics Laboratory of the National Oceanic and Atmospheric Administration (Pacanowski et al., 1991). The model domain extends over the world ocean from 80°S to 80°N with a uniform spatial resolution of 2° longitude and 1° latitude. There are 12 vertical levels (Table 1), which are chosen to coincide with the inflection points of the eleventh baroclinic mode of horizontal velocity corresponding to the mean temperature-salinity profile of the global ocean (Levitus, 1982). (These depths also 1011[',111]" correspond to those 11 SC'(1 by Bryan et al. [1975].) The relatively coarse resolution was chosen so as to facilitate experimentation (simulation and, later,

assimilation). The model has realistic topography and coast lines as shown in Figure 1. All horizontal boundaries are treated as impermeable with no slip boundary conditions. Conventional Laplacian operators are used for horizontal and vertical mixing, with constant coefficients. An additional local vertical mixing is performed to remove any statically unstable profiles.

The model is first spun up for 8 years forced by climatological monthly winds (Hellerman and Rosenstein, 1983) and by relaxation of its surface temperatures and salinities to monthly Levitus' (1982) values. The initial condition is at rest with a temperature and salinity distribution of Levitus (1982). Following the 8-year spinup, the model is forced by daily surface winds and climatological monthly heat flux from January 1992 to February 1996. The winds and heat flux are based, respectively, on the National Meteorological Center's 1000 mbar analysis using the formula of Wu (1982) and on the Comprehensive Ocean-Atmosphere Data Set (COADS) (Slutz et al., 1985; Woodruff et al., 1987) compiled by da Silva et al. (1994).

The skill of such model in simulating the ocean has been demonstrated in the past. For instance, a similar model was recently used by Chao and Fu (1995) in comparing model simulated sea level and measurements of TOPEX/POSEIDON. Differences between the present model and that of Chao and Fu (1995) include vertical resolution, vertical mixing formulation, and heat flux forcing, with the last being the most notable. Namely, Chao and Fu (1995) used time-invariant shortwave and longwave radiation, where in fact shortwave radiation has the largest annual cycle (see Section 3.3). The use of time-invariant shortwave radiation was one of the reasons for weak annual sea level variability in Chao and Fu (1995).

3. Results

To resolve all significant frequencies of the model, instantaneous values of sea level, as well as stream function, were saved at 12-hour intervals for analysis. Other prognostic variables (temperature, salinity, baroclinic velocity) were saved at 24 hour intervals, because, as analyzed below, they are dominated by lower frequencies. Under the rigid-lid approximation, sea level is computed hydrostatically from the surface pressure, of which the gradient is diagnosed from the equations of motion (See Appendix and Pinardi et al., 1995). The gradient operator is inverted using a conjugate gradient

method and surface pressure is solved apart from an unknown global constant, which is set to zero by assuming that the global sea level of the model remains time-invariant.

3.1 Trends in the Model Solution

Apart from variabilities due to temporal changes in the forcing, the model simulation exhibits a trend in several locations. Figure 2 compares the standard deviation of model sea level with and without the trend as well as the trend itself. The trend is as large as 10 cm/year (!) at several locations and is obviously unrealistic. This trend is due to the continued spin-up of the model, the change in wind stress from climatology to NMC analyses, and the imbalance between the prescribed heat flux and the model's mean heat transport divergence. To diagnose these differences, the model was rerun from January 1, 1992, with the same climatological wind forcing as the 8-year spin-up phase, but forced with the same COADS heat flux. The resulting trend is also shown in Figure 2-d. Differences between Figures c) and d) are due to the spin up by the winds whereas similarities are due to effects of the prescribed heat flux. There are different regions where surface heat flux or winds are the dominant forcing for the trend, but on average both forcing fields result in significant trends in the model over the two year simulation period.

A large part of the trend due to spin-up by the winds will become negligible over 10s of years by wave propagation and frictional dissipation, but that due to changes in mean heat flux will occur on a much longer advective-diffusive time-scale of order 100s of years. Worse yet, the prescribed heat flux induced trend will cause the surface waters to eventually boil or freeze in some regions due to the imbalance of heat flux in the surface layers. A common remedy to the diabatic trend is to alter the heat flux by damping surface (or other) temperatures and salinities towards realistic values (e.g., Han, 1984). Yet the heat flux imbalance is partially due to errors in the model formulation which such correction does not account; e.g., the model lacks resolution to support the large poleward heat transports of western boundary currents, nor is the mixed layer dynamics explicitly simulated in the present model. Therefore, rather than attempting to correct these errors, we shall accept the fact that the model has unrealistic trends due to model deficiencies and will analyze the variability apart from such trend. Such treatment is sensible to the extent of linear dynamics which is a reasonable approximation for the scales of interest in the present study. The analysis in the remainder of this study are based on detrended model results.

5

3.2 Frequency Spectra

The shape of the model sea level's frequency spectrum is primarily a function of latitude, and its zonal mean is shown in Figure 3 in energy preserving form. The annual harmonic dominates latitudes between 40°S and 60°N. In comparison higher latitudes have comparatively more energy in higher frequencies than do lower latitudes. The prominence of high frequency sea level fluctuations is also shown in Figure 4 as the half-energy period of the intra-seasonal variability (periods shorter than 180 days). There are vast areas in mid- to high-latitudes, especially in the Atlantic Ocean, where half the intra-seasonal sea level variability occurs at periods less than 20-days. Such high frequency variations are also evident in in situ measurements. Figure 5 compares sea level frequency spectra of tide gauges and model at typical mid-ocean stations in the tropics and high latitude. The shape and energy level are comparable between model and tide gauges. The half intraseasonal energy period at the two stations are 87.4 and 9.9 days, respectively. (The corresponding half energy period of the total energy is 466.0 and 21.3 days.) The tide gauge at Kerguelen Island exhibits a large amount of energy beyond 5-days, whereas the model energy decreases. This is due to the model's coarse resolution that does not resolve high frequencies and is disussed further in Section 3.5.

The validity of the model's high frequency variability can also be inferred from a comparison with altimetric data. For instance, Figure 6 compares the model simulation with TOPEX/POSEIDON data, and shows the amount of data variance explained by the model. Comparisons between data and model are made every 12 hours, assuming the data collected within 6-hours prior and after the model time step are contemporaneous and coincident with the model at that instant. The explained variance is positive over most of the 1-year period, demonstrating the model's skill. Also shown by the thick curve, is the difference of this 12-hourly comparison with another but performed in 3-day intervals assuming data within 1.5 days of the model time-step are coincident. The fact that the 12-hourly skill is better than the 3-day comparison demonstrates the presence of fluctuations in the TOPEX/POSEIDON data that have time-scales shorter than three days, and also the skill of the model in resolving them. Plate 1 shows the geographic distribution of this 12-hour minus 3-day skill. Most of the improvement occurs at high latitudes, consistent with the findings of the relative dominance of high frequency variability at these locations (Figures 3 and 4).

The presence of large-scale sea level variabilities with periods shorter than 10-days prompts some concern regarding the sampling characteristics of TOPEX/POSEIDON and analysis of its observations. Although the satellite's individual measurements are instantaneous and made continuously in time, geographically, the repeat period is 10-days. And, even though the satellite has a shorter three-day subcycle, its Nyquist frequency still falls shorter than the satellite three-day subcycle, its Nyquist frequency still falls shorter than the half intra-seasonal energy period in many locations (Figure 4). TOPEX/POSEIDON data are often mapped to regular latitude-longitude grids for analysis by space-time averaging, but such procedures can significantly filter out or worse yet alias the fast large-scale variability.

The dynamic nature of these differences in spectral characteristics are investigated further in the following sections.

3.3 Dependence on Forcing

The physical nature of the simulated sea level variability can be assessed by examining its dependence on the forcing field. The simulation was repeated by forcing the model with either time-varying wind or heat flux alone, keeping the other forcing constant in time. Figure 7 shows the geographic distribution of the rms sea level variability due to wind forcing and eating, as well as the percentage of the latter variance to that of the total. Effects of heating and cooling on sea level are largest at midlatitudes, especially near western boundary currents in the northern hemisphere, but is small in the tropics and the Southern Ocean (Figure 7a). These steric changes are in general smaller than the wind-driven variability, but are comparable around 30°S and dominating about 30°N (Figure 7c). Globally averaged, the effects of heating and cooling on sea level variability account for 27% of the simulated variability.

Changes in steric sea level are primarily due to seasonal changes in shortwave radiation. Figure 8 shows the rms amplitude of different components of COADS heat flux. Variability in shortwave radiation is dominant over most area with latent heat flux being prominent in the Kuroshio and Gulf Stream regions. Changes in net heat flux are largest in the western boundary currents of the northern hemisphere due to the seasonal variability of air-sea exchange (latent and sensible heat flux) and smallest in the tropics. In other regions, the amplitudes of heat flux variability are fairly uniform. Sea level variability due to changes in heat flux (Figure 7a) largely reflect the amplitude of heat flux change, including the north-south asymmetry, except in the Southern Ocean. The small amplitude of the heat-flux driven sea level change in the Southern Ocean, despite

its significant heat flux variability (Figure 8c), is primarily due to the smaller thermal expansion coefficient (Figure 9a). Amplitudes of steric sea level change was estimated directly from magnitudes of the heat flux (Figure 8c) using the time-mean thermal expansion coefficient at the surface (Figure 9b). Apart from some detailed structure due to advection and how heat is stored in depth, the gross similarities with the actual simulation (Figure 7a) is apparent. (Specific heat is practically uniform over the globe.)

Figure 10 compares the globally averaged frequency spectra of the wind and heat-flux driven sea level variability. (The two do not add to the total sea level energy because wind and heat flux variability are correlated.) Because monthly climatology of COADS is used in forcing the model, the simulated sea level fluctuations due to heating/cooling is limited to seasonal changes (annual harmonic). Globally averaged, heat flux and wind-driven sea level variability are of comparable magnitude at the annual period. (The annual harmonic, on average, accounts for 13% of local sea level variability.) Figure 10b shows the ratio of heat-flux driven sea level variability to the sum of the two variance for the annual cycle. Heat flux induced sea level changes dominate the annual cycle north of 20°N and between 20°S and 40°S in the southern hemisphere, but is insignificant elsewhere.

3.4 Vertical Structure

It is instructive to examine the ver tics) structures of the temporal changes so as to further diagnose the dynamic nature of sea level variability. (See Appendix for how tile.sc decompositions are performed.) Heat-flux driven variability is largely due to changes near the surface. Figure 11 shows variability in steric sea level due to changes in the top two levels of the model. The near surface temperature and salinity changes (Figure 11) account for nearly all the heat flux induced sea level variability (Figure 7a).

Analysis of wind-driven variability is most revealing by separating barotropic contributions from baroclinic changes. Although varia blk · topography and nonlinearities render the equations of motion nonseparable, and thus each mode dynamically dependent on another, dynamic modes locally form a complete orthogonal basis function onto which variables can be expanded. Figure 12 compares wind-driven sea level variability due to changes in barotropic and baroclinic circulation. There is a clear delineation in space of which component dictates wind-driven sea level fluctuations (Figure 12c). Sea level variability is dominated at high latitudes by changes in the barotropic circulation, whereas it is due primarily to baroclinic changes in the tropics and along continental

8

marginsintemperate latitudes. The latitudinal separation that delineates barotropic and baroclinic dominance occurs between 20° to 30° from the Equator.

This spatial difference of barotropic and baroclinic dominance of sea level variability largely explains the latitudinal dependence of the shape of sea level's frequency spectra seen earlier (Figure 3, 4). Baroclinic variability is characterized by low-frequencies with periods typically longer than 100 days whereas high frequency changes dominate barotropic fluctuations with periods even shorter than 10 days (Figure 12d). Supporting evidence for the existence of such large-scale, high frequency, barotropic fluctuations can be found, for example, in bottom pressure measurements. For instance Hughes and Smithson (1996) show an example of remarkable coherence in bottom pressure over 350 km in the South Atlantic.. Eubanks (1993) illustrates an example of coherent bottom pressure observations over 2000 km in the north central Pacific which are correlated to atmospheric forcing (Luther et al., 1000).

Differences in latitudinal structures of barotropic and baroclinic changes arise from properties of wind forcing and that of ocean dynamics. Figure 13 shows the total variance and frequency spectra of wind stress curl. Variabilities of wind stress curl are largest in high latitudes, and is nearly white in frequency spectra except near the equator where it is slightly more red. The response of the ocean to changes in external forcing depends to a large extent on the properties of the planetary waves that can propagate energy away from the forcing area. In particular, Rossby waves have a maximum frequency when zonal wave length equals the Rossby radius times 2π. For baroclinic waves, the deformation radius is typically tens of kilometers at mid-latitudes which is much smaller than what the present model resolves, which is about 2000 km (approximately ten times the zonal resolution), Thus the model's baroclinic response has a maximum frequency dictated by model resolution. The barotropic Rossby radius, on the other hand, is larger than this model limit almost everywhere. Figure 14 shows the minimum period of free planetary waves that the model can resolve, and the corresponding variance of wind stress curl with periods longer than this limit that are responsible for driving the resolved waves. Forcing of baroclinic Rossby waves are limited primarily in the tropics despite the large variability in winds at high latitudes. Because of the wider frequency window available for barotropic planetary waves, the spatial distribution of barotropic forcing is similar to the total forcing (Figure 13) and is largest at high latitudes.

3.5 Wind-Driven Barotropic Changes

The pattern of wind-driven barotropic sea level variability (Figure 12a) is strongly influenced by bottom topography (Figure 1). Figure 15 shows spectra of sea level and wind stress curl at two locations where barotropic variability is large (Figure 12a). Despite the spectra of wind-stress being dominated by higher frequencies and being indistinguishable from each other (Figure 15b), sea level spectra at the two locations are quite different; Sea level over the Mid Indian Ocean Ridge is predominantly fluctuations with periods shorter than 10 days, while the Bellingshausen Abyssal Plain is dominated by variability with periods longer than 30-days. Plate 2 compares barotropic sea level variability with periods shorter and longer than 20 days, with contours of f/H superimposed. The largest variabilities are bordered by large gradients of f/H. Variability in the Bellingshausen Abyssal Plain stands out as the outstanding feature at lower frequencies, whereas enhanced higher frequency variabilities occur along the mid ocean ridges of the Southern Ocean, in particular along their eastern flank.

Coherence between barotropic sea level and wind stress curl is also shown in Plate 2 at two frequencies representative of the two frequency bands above. Sea level is coherent with the wind at 30-days in the Bellingshausen Abyssal Plain with a nearly zero phase lag (not shown). In comparison, coherence between the two is only marginally significant along the ocean ridges at 10- days where the sea level variability is large. The regions of significant coherence are in rough agreement with those where the intra-seasonal, large-scale sea level variability can be explained to some extent by the linear barotropic vorticity dynamics (Fu and Davidson, 199[]).

Leipold (1983) examined dynamics of a resonant barotropic response in regions of closed j/H contours, suggesting a balance between vorticity input by wind-stress and changes in relative vorticity with a feedback by the baroclinic bottom torque. However, predicted periods of such oscillations are in the range of 50 days to several years, and is much longer than the present variability. In addition Leipold (1983) predicts a 900 phase lag between sea level and wind stress curl. Instead, our model's barotropic response in the Bellingshausen Abyssal Plain may be enhanced by resonant Rossby wave basin modes. For a simple rectangular basin with east-west and north-south dimensions of L_1 and L_2, respectively, frequency of such resonance is given by (Willebrand et al., 1980),

$$\omega = \frac{\beta}{2} \left[\left(\frac{m\pi}{L_1} \right)^2 + \left(\frac{n\pi}{L_2} \right)^2 + \frac{f^2}{gH} \right]^{-1/2}$$

10

$$m, n = 1, 2, \ldots$$

Approximating the Bellingshausen Abyssal Plain by a rectangular basin with characteristic dimensions of $L_1 = L_2 = 2000$ km, the minimum period of such resonance occurs at 28 days, comparable with the enhancement seen in Figure 15. Other abyssal plains, such as the Wilkes ($\approx 110°E$, $60°S$), Argentine ($\approx 45°W$, $40°S$), and Weddell Abyssal Plains ($\approx 30°W$, $65°S$) are also dominated by lower frequencies suggestive of such basin modes (Figure 4), but their energy content is small (Figure 12), possibly due to dissipative effects owing to the geometry (they are smaller in size and not as isolated as the Bellingshausen Abyssal Plain).

The enhanced high-frequency variability along the axis of the Southern Ocean ridges occur in regions of semi-open f/h contours, and are likely a result of western intensification of interior fluctuations rectified by bottom topography (Pedlosky, 1987). The shape of their spectra are similar to the interior ocean (Figures 3 and 15a). Its spectral level decreases beyond 5 days owing to the resolution of the model (Figure 15a) as described in Section 3.4.

Evidence for such resonance was sought in the TOPEX/POSEIDON data by comparing it with model results in the two high variability regions (Plate 3). In the Bellingshausen Abyssal Plain, there is a slight enhancement of energy near 30-days which appears coherent with the model, but the amplitude of T/P data is much smaller than the model simulation. In comparison, T/P data along the Mid Indian Ocean Ridge is comparable to the model simulation with similar spectral characteristics. Both regions overlap the high eddy variability area associated with the Antarctic Circumpolar Current, and therefore large-scale high frequency changes are difficult to discern from contributions of meso-scale eddies. Nevertheless, the comparisons suggest that planetary basin modes in the Bellingshausen Abyssal Plain may not be excited as strongly in the real ocean as in the model. This may be due to the limited resolution of the model. Namely, the model's vertical resolution at depth is as large as 1000 m (Table 1), whereas the actual height of mid ocean ridges changes more gradually and therefore does not form as strong a boundary in f/H as in the present model. A model simulation with 20 vertical levels indeed shows sea level coherent with TOPEX/POSEIDON observations with more comparable magnitudes (Fu and Smith, 1996).

11

3.6 Wind-Driven Baroclinic Changes

Spectral analysis shows that the model's wind-driven baroclinic sea level variability is dominated by the annual harmonic at most locations. Figure 16a shows the rms of sea level at the annual period, which is hardly distinguishable from Figure 12b. Wind-driven baroclinic sea level changes are generally largest between 15 and 20° of" the Equator rather than within the equatorial wave guide. This suggests processes other than equatorial waves as the primary mechanism underlying these changes. In contrast the total variance of baroclinic sea level with periods between 10 and 100 days (Figure 16b) is maximum along the Equator elucidating the prominence of Equatorial waves at higher frequencies.

Plate 4 shows coherence and phase between wind-driven baroclinic sea level and wind stress curl at the annual period in regions where the former is large (Figure 16). Generally speaking, places of largest variance have significant coherence between sea level and local wind stress curl, such as along ~18°N in the Pacific and ~18°S in the Indian Ocean. In these regions, sea level leads (lags) wind stress curl by 90° in the northern (southern) hemisphere suggestive of wind-driven planetary wave dynamics.

Regions where coherence with wind stress curl is not significant suggests dynamics other than local wind stress curl to be important, such as propagating waves from remote locations. Plate 5 shows coherence at the annual period between Lame.lillic. sea level at 94° w 9° s (asterisk) > where coherence between sea level and wind stress curl is low (1'late 4A), and sea level at other locations. A characteristic arc of high coherence is found near 94°W 9°S and along the eastern boundary of the North and South Pacific and along the Equator between 140°W and 100°W. The phase leads that at 94°W 9°s along the Equator and along the eastern boundary away from the Equator, suggestive of Equatorial waves (Kelvin) impinging on and reflecting from the eastern boundary. Large coherence is also found in other locations, but their significance maybe questionable given the relatively short duration of the simulation. Interestingly, regions of high coherence in Plate 5 generally coincide with places of low coherence with the local wind stress curl (1'late 4).

Further insight into the dynamics of wind-driven baroclinic sea level changes can be attained by decomposing the model state into different baroclinic modes. The dependence of sea level (surface pressure) on baroclinic anomalies is primarily due to effects of density changes through the hydrostatic relation. Baroclinic velocity in turn

12.

is related to sea level through geostrophy, but only weakly as an independent prognostic variable (Appendix), and therefore its effects are not examined below.

Amplitudes of vertical displacement were estimated from changes of density in the purely wind-driven simulation (section 3.2), which were then expanded into different dynamic modes. Since density changes near the surface are strongly influenced by horizontal advection and diabatic effects, near-surface displacements were estimated by linear extrapolation from values below. The base of this extrapolation was estimated to be the near surface depths where amplitudes of the horizontal velocity's first baroclinic modes are nearly constant (within 90% of its surface value). These levels were generally the second or third model levels and roughly correspond to typical depths over which convective adjustments frequently occurred (mixed layer). Sea level due to different baroclinic modes were in turn estimated from the implied density changes of the separate modes.

Figure 17 compares sea lewd variability clue to the first and second baroclinic modes. The first baroclinic mode dominates the baroclinic contribution to sea level fluctuations; it accounts for much of the zonal structure in the Indian Ocean ($\sim$ '20"s) and the North Pacific ($\sim$ 15 °N), as well as the highs in the western Equatorial Pacific and Atlantic Oceans. The second mode is comparable or larger than the first in the eastern tropical Atlantic and Equatorial Indian Oceans (Figure 17c), but their magnitudes are relatively small (Figure 17b).

The relative dominance of the second mode to the first in the equatorial Atlantic and Indian Oceans is consistent with observations. The nature of this difference is partly due to the relative magnitude of forcing of the separate dynamic modes as a result of geographic differences in stratification. Wind forcing is applied to the model as a body force at the top most level and zero elsewhere. Figure 18 compares the relative magnitude of forcing for the two baroclinic modes by expanding such forcing profile into different modes. Both modes are most efficiently forced in the tropics, which is another reason for the dominance of baroclinic changes in low latitudes (Figure 12) in addition to the relative energy content in the Rossby wave band (Figure 14). The ratio of the two shows that the second mode is more efficiently forced in the eastern tropical Atlantic and Equatorial Indian Oceans, consistent with the findings of their relative strengths.

13

3.7 Energetics

The preceding sections analyzed variabilities of the simulated circulation in terms of sea level, focusing on the direct physical relationship between sea level and independent model variables. However, there are aspects of the circulation that this relationship is only weakly dependent on or independent of, such as baroclinic velocity changes (Appendix). Therefore, for completeness, we shall briefly examine aspects of the model circulation itself in terms of its energetics.

Plate 6 compares the model's depth integrated available potential energy (APE) due to wind forcing in different dynamic modes. The pattern of total APE is similar to that of the baroclinic sea level changes (Figure 12b) but the relative magnitude of the second mode to the first is more significant than that in the case of sea level (Figure 17b). This is because the second baroclinic mode displacements have opposite signs in the upper and lower water column, which makes their contribution to sea lewd relatively small in comparison to the mode's energy content. Energy-wise, the first and second modes are as nearly significant as each other in the tropics, but elsewhere the first mode, albeit small in magnitude compared to the tropics, dominates the APE.

The modal decomposition of model kinetic energy (KE) is shown in Plate 7. Kinetic energy is dominated by the baroclinic circulation in the equatorial region, with increasingly less energy in higher baroclinic modes and away from the Equator. Although sea lewd changes due to the barotropic mode at mid- and high-latitudes were comparable to baroclinic sea lend changes in the tropics (Figure 1 2), the actual KE content of the former is relatively small compared to those of the baroclinic Equatorial flue.tuatiolls. This is in part clue to the latitudinal dependence of the Coriolis parameter. Ye%, as for sea level, local KE is dominated by barotropic circulation at latitudes beyond 20° of the Equator (Willebrand et al., 1980), whereas baroclinic changes are dominant within the tropics.

4. Summary and Conclusion

Characteristics of large-scale sea level variability from periods of days to a year were analyzed over the global ocean based on numerical simulations and comparing aspects of it with TOPEX/POSEIDON and tide gauge measurements. Salient geographic variability of o c ean dynamics underlying sea level fluctuations is revealed by decomposing model results into different causal effects and spectral (frequency and dynamic) modes.

14

At IJlicl-latitudes, large-scale sea level variability is primarily due to steric changes associated with the seasonal heating and cooling cycle. These changes are confined to the surface layers of the model and dominate the annual cycle. In comparison, changes in the tropics and high latitudes are mainly wind-driven. This is due to the weak seasonal cl iai iges of tropical h eat flux and to the small thermal expansion coefficients at high latitudes.

The nature of wind-driven variability itself exhibits a strong latitudinal dependence. Wind-driven changes are largely baroclinic in the tropics but barotropic at higher latitudes. These reflect the latitudinal dependence of the Coriolis parameter and the relative energy content of wind stress cur] in tile respective planetary wave frequency and wave number bands. Further analysis shows that baroclinic changes are dominated by the annual harmonic of the first baroclinic mode and is largest off the Equator. Variabilities associated with equatorial waves are much smaller than these off-equatorial seasonal barocl inic adjustments.

Wind driven barotropic changes exhibit a notable enhancement over several abyssal plains in the Southern Ocean. These regions, the Bellingshausen Abyssal Plain in particular, are semi-encl osed with (list.c)llltillllliticsill potential vorticity that allow resonant planetary wave modes to exist. Otherwise, barotropic sea level changes are typically dominated by high frequen cies with as much as half the total variallc.till periods shorter than 2(I days, reflecting the general frequency spectra of wind-stress curl.

The model's frequency spectra were shown to be qualitatively similar to altimetric and tide gauge measurements. Establishing reliability of other aspects of the model is not trivial as observations with comparable sampling are not readily available. Wunsch (1996) has recently examined the issue of vertical modal decomposition of oceanic variability based on historical moored current meter data. To the extent motions are in geostrophic balance, surface velocities are equivalent to the slope of sea level and therefore the two studies are comparable. Although results at high latitudes are consistent between the two, a quantitative statement is difficult to make. Differences between current meter data and the present model simulation can be due to contributions from m e soscale eddies to the former but which are absent froi n the present study. Further systematic testing of the m odel is required to establish the quantitative reliability of the present results. At the same tiquantifying effects of missing m odel physics is essential in performing such comparisons.

The present study suggests geographic variations in the nature of sea level variability of the global ocean, which in turn indicate difficulty in directly inferring circulation from sea level measurements alone. There is no uniformly applicable pointwise correspondence between sea level and instantaneous circulation at depth. Although some relation with latitude exists, it is strongly modulated by the effects of coastal geometry, bottom topography, and stratification that result in strong inhomogeneities and anisotropy.

What has been analyzed here is the instantaneous direct forward physical relationship between independent prognostic model variables and sea level. However, other physics can be born upon the problem of inferring circulation from sea level measurements. For instance, temporal evolution of sea level contain additional information regarding the underlying three-dimensional circulation, which has not been addressed here. This is a problem of observability, and such inference is one of the subjects and purposes of assimilation. The present analysis points to a minimum set of dynamics necessary to resolve the dominant variability of sea level and thus to invert it,; These are near surface steric effects and adiabatic first baroclinic and barotropic changes in circulation.

Finally, the presence of high frequency barotropic sea level variability at high latitudes poses a potential sampling problem in analyzing satellite altimetry data. The Nyquist frequency of TOPEX/POSEIDON is 20-days which is larger than the central period of sea level variability in many regions of the Southern Ocean. Altimetric data are frequently mapped onto regular grids for analysis by interpolating along-track data in space and time which could potentially alias the energetic high frequency variability. The present study suggests that analysis and therefore assimilation is best performed using along-track rather than statistically mapped data to avoid such problems. Such effort is presently underway and will be reported elsewhere. `

Acknowledgment

Appendix: Decomposition of Sea Level

Under the rigid-lid approximation, model sea level is evaluated from surface pressure against the rigid-lid using the hydrostatic relationship. Sea surface pressure in turn is computed diagnostically from the model prognostic equations.

In time-stepping the model, sea surface pressure ($p(0)$) is typically eliminated from the prognostic integration by solving the depth dependent (baroclinic) and the depth averaged (barotropic) part separately. The depth dependent pressure anomaly ($p'(z) = p(z) - \int p(z)dz/H$) is solved by the hydrostatic relationship. The gradient of the depth averaged pressure anomaly ($\int p(z)dz/H = p(0) - p'(0)$, i.e., sea sill.faCc! pressure minus the surface value of the depth dependent pressure anomaly) is eliminated from the calculation by taking the curl of the depth averaged momentum equation, which flow is horizontally nondivergent. However, once all prognostic variables are time-stepped, the surface pressure gradient can be evaluated since all other terms of the equations of motion, in particular the surface momentum equation, are known including the time-derivatives. Surface pressure is computed by inverting the gradient operator up to an unknown constant, which from volume conservation is typically set to zero; viz., anomaly from global mean.

The model sea level (η) can therefore be thought Of as a function of the three-dimensional model prognostic state (temperature T; salinity S; zonal velocity U; meridional velocity V);

$$\eta = S(T, S, U, V) \tag{J}$$

where function S denotes the sea level talc.ulaticn] described above. Namely, S stands for integrating the model for one time-step, diagnosing surface pressure gradient, inverting the gradient operator, and converting pressure to sea lewd.

Sea level due to various aspects of the model can be evaluated using this diagnostic algorithm. For example, sea level anomaly due to changes in barotropic circulation can be computed by,

$$S(T, S, U_{bt} + U, V_{bt} + V) - S(T, S, U, V) \tag{2}$$

where the overbar denotes time-mean and subscript bt den otes barotropic anomalies. Other anomalies can be computed likewise. Note however that because the governing equations are nonlinear, the sum of different anomalies about the referen ce mean do not strictly equal the original sea level. However, for the anomalies in the examples discussed here, the relation is nearly linear.

Finally, as an independent prognostic variable, baroclinic velocity has little contribution to sea level anomaly. Baroclinic velocity directly affects sea level calculation through the barotropic equation. Although baroclinic velocity has zero vertical mean 1 by definition, the verti cal mean of its square (advect ion term) is not necessarily zero. 1 lowever, in practice such contribution is small. This of course does not mean that there is no correlation between sea level and baroclinic velocity; because of the dominant geostrophic balance that exists, baroclinic velocity is correlated to density changes which in turn determines baroclinic pressure.

References

Bryan, K., S. Manabe and R. C. Pacanowski, 1975. A global ocean- atmosphere model. Part II. The oceanic circulation, *Journal of Physical Oceanography, 5*, 30- 46.

Chao, Y., and 1,.-1,. Fu, 1995. A comparison between the TOPEX/POS EIDON data and a globs] ocean general circulation model during 1992- 1993, *Journal of Geophysical Research, 100,* 24,965 24,976.

Eubanks, T. M., 1993. Interactions between the atmosphere, oceans and crust,: possible oceanic signals in earth rotation, *Advances in Space Research,* 13 (-1 1) , (1])291- (11)300,"

Ezer, 'J'., and G. J,. Mellor, 1994. Continuous assimilation of Geosat altimeter data into a till'CC-clilllCllsiC)llal primitive equation Gulf Stream model, *Journal of Physical Oceanography, 24, 832-847.*

Fu, 1,.-1,,, and R. A, Davidson, 1995. A note on the barotropic response of sea level to time-dependent wind forcing, *Journal of Geophysical Research,* 100, 24,955-24,963.

Fu, L.-L., and R. D. Smith, 1996. Global ocean circulation from satellite altimetry and high-resolution computer simulation, (unpublished manuscript).

Gill, A. E., and P. P. Niiler, 1973. The theory of the seasonal variability in the ocean, *Deep- Sea Research*, **20**, 141-177.

Han, Y.- J., 1984. A numerical world ocean circulation model. Part II A baroclinic experiment. *Dynamics of Atmospheres and Oceans*, **S**, 141- 172.

Hughes, C. W., and M. J. Smithson, 1996. Bottom pressure correlations in the South Atlantic, *Geophysical Research Letters*, **23**, *2243-2246*.

Leipold, G., 1983. Vorticity oscillations over closed-f/H contours, *Hamburger Geophysikalische Einzelschriften*, 94pp.

Levitus, S., 1982. Climatological Atlas of the World Ocean, *NOAA Prof. Pap.* **13**, Washington, DC, 173pp.

Luther, D. S., A. D. Chave, J. H. Filloux, and P. F. Spain, 1990. Evidence for local and nonlocal barotropic responses to atmospheric forcing during BEMPEX, *Geophysical Research Letters*, *17*, 949 952.

Oschlies, A., and J. Willebrand, 1996. Assimilation of Geosat altimeter data into an eddy-resolving primitive equation model of the North Atlantic Ocean, *Journal of Geophysical Research*, **101**, *14175 14190*.

Pacanowski, R., K. Dixon, and A, Rosati, 1991. Modular Ocean Model Users' Guide, Ocean Group Tech. Rep. 2, Geophys. Fluid Dyn. Lab., Princeton, N.J..

Pedlosky, J., 1987. *Geophysical Fluid Dynamics*, 2nd *cd.*, Springer Verlag, New York.

Pinardi, N., A. Rosati, and R. C. Pacanowski, 1995. The sea surface pressure formulation of rigid lid models. Implications for altimetric data assimilation studies, *Journal of Marine Systems*, **6**, 109 119.

da Silva, A. M., C. C. Young, and S. Levitus, **1994**, Atlas of Surface Marine Data 1994, Volume 3: Anomalies of Heat and Moment um Fluxes, NOAA Atlas NESDIS 8. U.S. Dept. Commerce, NOAA, NESDIS.

Slutz, R. J., S. J. Lubker, J. D. Hiscox, S. D. Woodruff, R. L,. Jenne, D. H. Joseph, P. M. Steurer and J, D. Elms, 1985. COADS, Comprehensive Ocean-Atmosphere Data Se%, Release 1. Climate Research Program, Environmental Research Laboratory, Boulder, CO, 262pp.

Stammer, D., R. Tokmakian, A. Semtner, and C. Wunsch, 1996. How closely does a 1/4° global ocean circulation model simulate large-scale observations?, *Journal of Geophysical Research*, (in press).

Willebrand, J., S. G. H. Philander, and R. C. Pacanowski, 1980. The oceanic response to large-scale atmospheric disturbances, *Journal of Physical Oceanography, 10*, 411 - **429**.

Woodruff, S. D., R. J. Slutz, R. L. Jenne, and P. M. Steurer, 1987. A comprehensive ocean-atmosphere data Set, *Bulletin of the American Meteorological Society, 68*, *1239 1 250*.

Wu, J., 1982. Wind stress coefficients over sea surface from breeze to hurricane, *Journal of Geophysical Research, 87*, 9704-9706.

Wunsch, C., 1996. The vertical partition of oceanic horizontal kinetic energy and the spectrum of global variability, (unpublished manuscript).

Tables

Table 1: Depth of levels (z) and layer thicknesses (δz) used in the model. Units are in meters.

Plates

Plate 1: Geographic pattern of relative skill of the model simulation in simulating TOPEX/POSEIDON measurements. The values compare the skill of the model field at 12-hour and 3-day intervals. Positive values indicate larger skill (cm^2) with the 12-hourly comparison.

Plate 2: Barotropic sea level variability (cm) at periods longer (A) and shorter (B) than 2.0 days, respectively. The contours are of f/H (contour interval 10^7 (ms)$^-$ ʻ). Also shown in (C) and (D) are coherence between barotropic sea level and local wind stress curl at periods of 30-days and lo-days, respectively. Coherence larger than 0.3 is significant at the 95% confidence level.

Plate 3: Comparison of model and TOPEX/POSEIDON measurements in the high variability regions of wind-driven barotropic sea level changes of Figure 12 and Plate 2. Average sea level (cm) around points "B" and "W" in Figure 12 are shown in (A) and (B) for a 200 day period, corresponding to regions with rms sea level greater than 6 and 4.8 cm in plates 2A and 2B, respectively. Model (blue) output is shown at 24 hour intervals, whereas TOPEX/POSEIDON data (red) are average values at 3-day intervals based on along-track data. Corresponding frequency spectra are shown in (C) and (D).

Plate 4: Coherence (A) and phase (B) between wind-driven baroclinic sea level variability and wind stress curl at the annual period in regions where sea level standard deviation is larger than 1.5 cm (Figure 16). Coherence larger than 0.67 (yellow) is significant at the 95% confidence level. Positive phase indicates sea level leading wind stress curl.

Plate 5: Coherence (A) and phase (B) between wind-driven baroclinic sea level changes at 94 °W 9°S (asterisk) and the same at other locations. Coherence larger than 0.67 (yellow) is significant at the 95% confidence level. Positive phase indicates sea level at the asterisk leading.

Plate 6: Depth-integrated wi]]d-drive]) available potential energy (J/m^2); (A) total, (B) first baroclinic mode, (C) second baroclinic mode, (1)) % of total due to first baroclinic mode.

Plate 7: Depth-integrat ed wind-driven kinetic energy (J/m^2); (A) barotropic, (B) first Lame.lillic. mode, (C) second baroclinic mode, (D)% of total due to barotropic mode.

Figures

Figure 1: Mode] coastlines (thick) and bottom topography (thin). Contour interval for topography is 1000 m.

Figure 2: Model sea level variability; (a) root-mean-square sea level over the two-year simulation; (b) Same as (a) but a linear trend shown in c) has been removed; (d) Linear trend for same model simulation as (c) but forced with Hellerman and Rosenstein winds. Contour intervals are 2 cm (a, b) and 5 cm/year (c., d). Shaded

21

regions indicate absolute values larger than 4 cm (a, b) and 5 cm/year (c, d). Negative values are contoured by dashed curves in c) and d).

Figure 3: Shape of mean frequency spectra of sea level in variance-preserving form as a function of latitude. Means are computed by averaging spectra zonally normalized by total energy at each location; therefore the figure snows the average shape of the spectra. Contour interval is 10^{-4} with values la rger than 2×1 () ^{4} shaded. Units are arbitrary.

Figure 4: The figure shows the period above and below which half the intra-seasonal (period shorter than 180 days) sea level fluctuations occur. Contour interval is 10-days (saturated at 100-days). Regions with half energy period shorter than 20-days are shaded.

Figure 5: Frequency spectra (variance preserving) of tide. gauge records (thick) compared with the model equivalent (thin); (A) Diego Garcia (72.4°E, 7,3°S), (B) Kerguelen Island (70.'2°1<1, 49.4° S), Spectra are computed from daily tide--;auge records with atmospheric pressure correction assuming t] ie inverse barometer. Th e peak in the tide gauge record at (A) near 0.07 cpd is the fortnightly tide.

Figure 6: Model's skill in simulating TOPEX /POSEIDON measurements. The thin curve shows the amount of data variance (cm^2) explained by the model as a function of time. Also shown (thick curve) is the relative skill of this 12-hourly comparison over a three- day comparison.

Figure 7: Sea level variability (cm) as a function of forcing. The three figures correspond to sea level change due to heating and cooling (a) and wind stress (b), and the ratio (percentage) of the former variance to that of the total (c). Contour intervals are 1 cm, 2 cm, and 20%, respectively. Shaded regions denote areas with sea level standard deviation larger than 4 cm (a and b) and 50% (c.). The total sea level variability is shown in Figure 2b.

Figure 8: Standard deviation of COADS heat flux (W/m^2). Contour intervals are]() (W/m^2) for short wave (a) and latent heat fluxes (b), 5 (W/m^2) for long wave and sensible heat fluxes, and 20 (W/m^2) for the net heat flux. Shaded regions denote area larger than 50 (W/1112).

Figure 9: Thermal expansion coefficient at the surface (10^{-4} cm^3/°C) (a) and magnitude of steric sea level change estimated from net heat flux variability (cm) (b)). Contour intervals are 0.5 x 10^{-4} cm^3/° (a) and 1 cm (b), respectively. Shaded area in (b) correspond to regions larger than 4 cm as in Figure 7.

Figure 1 0: Comparison of the effects of heating/cooling and wind on sea level change; (A) Average shape of global frequency spectra normalized by total sea level variance in energy preserving for 111. (B) Percentage Of heating and cooling effects on sea level at the annual period. Contour interval in (B) is 20% with regions larger than 50% shaded in gray.

Figure 11: Sea level change due to density change of the top two levels of the model when forced by time-mean winds and climatological monthly heat flux.

Figure 1 2: Wind driven sea level change as a function of dynamic mode; (A) barotropic mode, (B) baroclinic mode, (C) percentage of (B) to total wind driven variability. Average frequency spectra of the two components are shown in (D) in variance preserving form normalized by the total variance. Contour intervals are 2 cm (A, B) and 25% (C). Shaded regions denote values larger than 4 cm (A, B) (as in Figure 7) and 50% (C). Asterisks denoted "W" and "B" in (A) are in the local maximum of sea level variability and are further examined in Section 3.5.

Figure 13: Variance (A) and frequency spectra of wind stress curl. Contour interval is 2×10^{-4} in (A) with regions larger than 2 x 10^{-4} shaded in gray. The frequency spectra is in energy preserving form and corresponds to averages between 60°S~40°S (thin) and 0°~20°N (thick).

Figure 14: Characteristics of planetary waves resolved by the model; Minimum period (class) that can be resolved for first baroclinic (A) and barotropic (B) Rossby waves. Total variance of wind stress curl within the period of (A) and (B) are shown in (C) and (D), respectively. Contour intervals are 100 days, 2 days, 3×10^{-3}, 10^{-4}, respectively. Shaded regions are larger than 365 days, 3 days, '2 x 1 0^{-13}, and 1 0^{-4}] respectively.

Figure 15: Spectra of sea level (A) and wind stress curl (B) at two locations shown as asterisks denoted "B" and "W" in Figure 12a. The two points are at (100°W,

60°S)(thick) and (108°E, *53° S)* (thin), in the Bellingshausen Abyssal Plain and on the mid Indian Ocean Ridge, respectively.

Figure 16: Variability (cm) of wind driven baroclinic sea level fluctuations: (A) annual period; (B) 10 to 100 day period. Contour intervals are '2 and 0.5 cm with regions larger than 4 and 1 cm shaded in gray, respectively.

Figure 1 'I': Sea level variability (cm) due to wind driven first (A) and second (B) baroclinic modes. Also shown in (C) is the ratio of (A) to (B). Contour intervals are 2 cm (A), 1 cm (B), and 0.5 (C). Regions larger than 4 cm are shaded in (A) and (B) as in Figure 12, and 0.75 for (C).

Figure 18: Relative magnitude of wind forcing for the first (A) and second (B) baroclinic modes in arbitrary units. The ratio of (B) to (A) is shown in (C). Contour intervals are 0.5 (A and B) and 0.25 (C), with regions larger than 3.0 (A and B) and 1.0 (C) shaded in gray.

	z(m)	Δz
1	?5	50
?	75	50
3	175	150
4	325	150
5	550	300"
6	850	300
7	1200	400
8	1700	600
9	2375	-/50
10	3?50	1000"
11	4250	1000"
12	5250	1000"

Table 1

Explained sea level variance (cn?)

60N
40N
20N
0
20S
40s
60s

o   60E   1201:   180   120W   60W   o

-10.   -5.   0.   5.   10
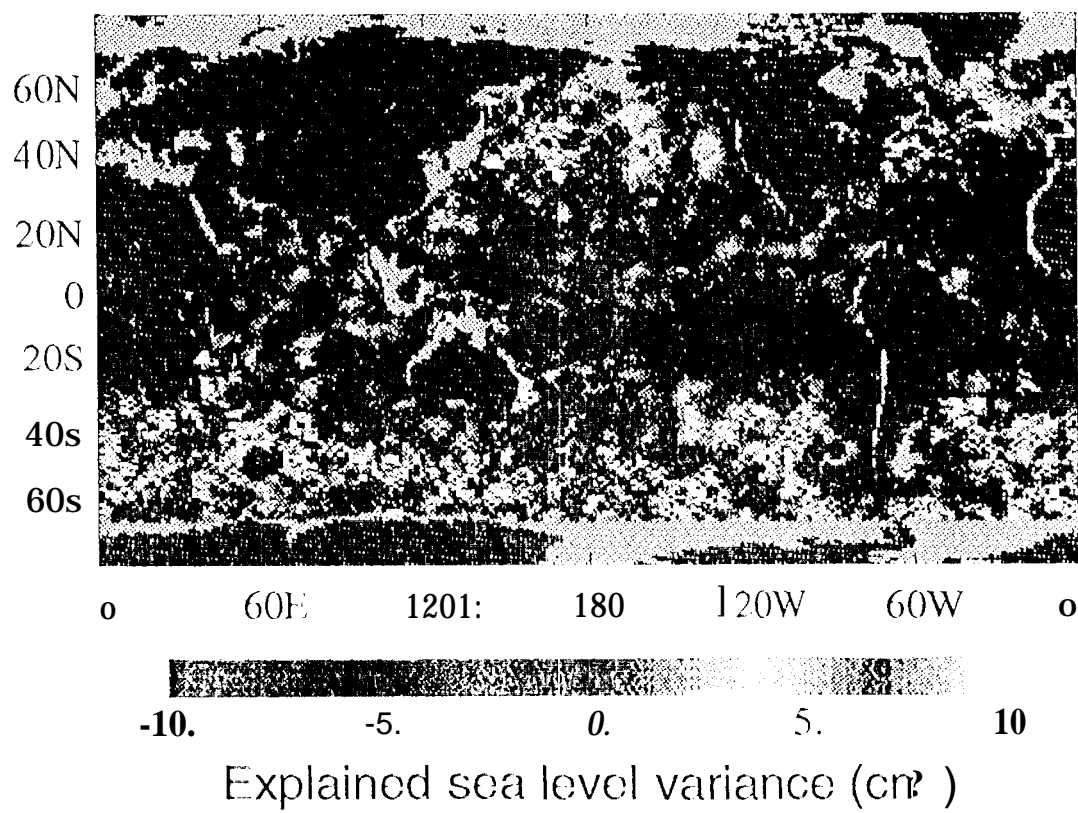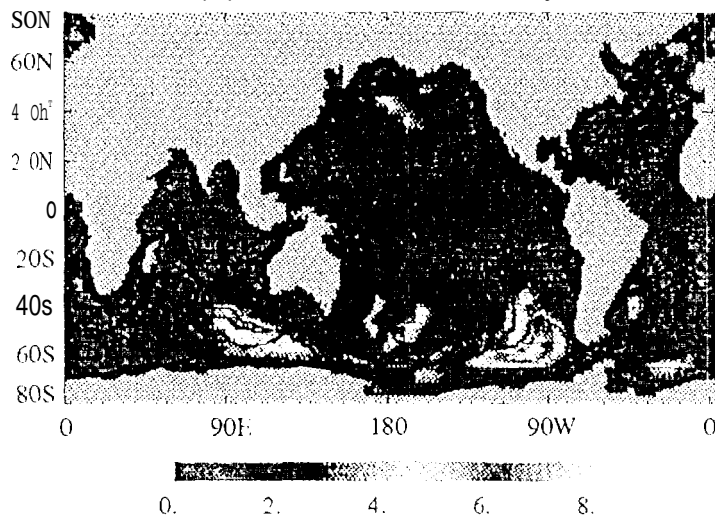
(A) RMS SSH (1 > 20 days)

(B) RMS SSH (1 < 20 days)
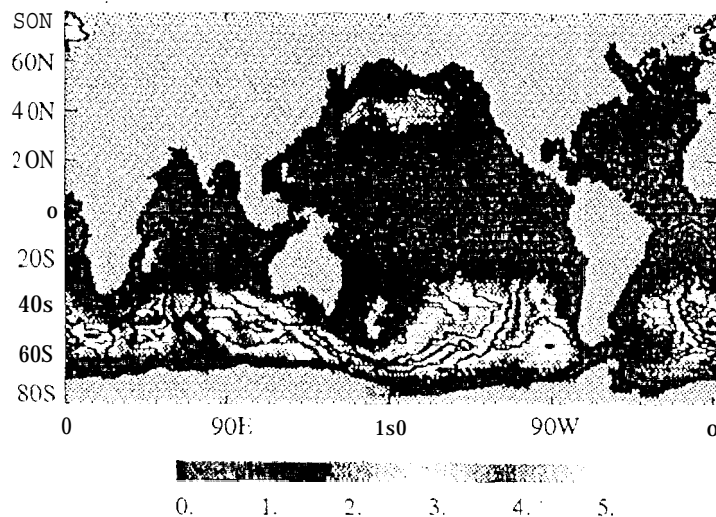
(C) COHE RE NCE (1 = 30 days)

(D) COHE RE NCE (-1 = 10 days)

(A) Sea level (region "U")

T/P

MODEL

YEAR DAY (1992)

(B) Sea level (region "W")

YEAR DAY (1992)

(C) spectra (region "H")

F REQUENCY (cpd)

(D) Spectra. (region "W")

FREQUE NCY (cpd)
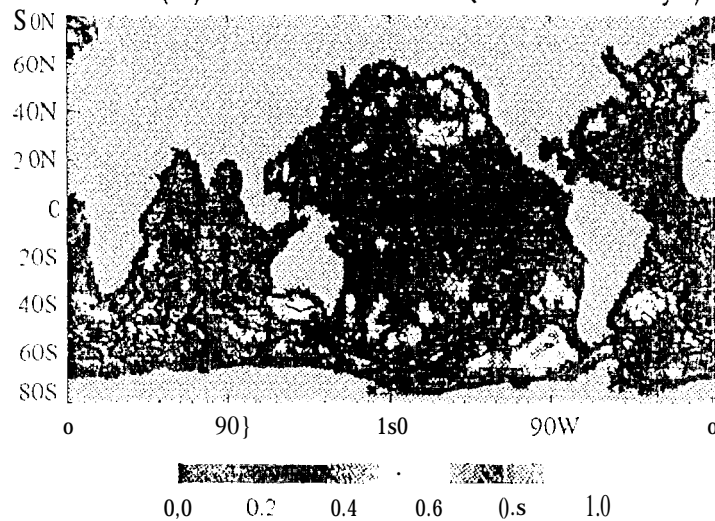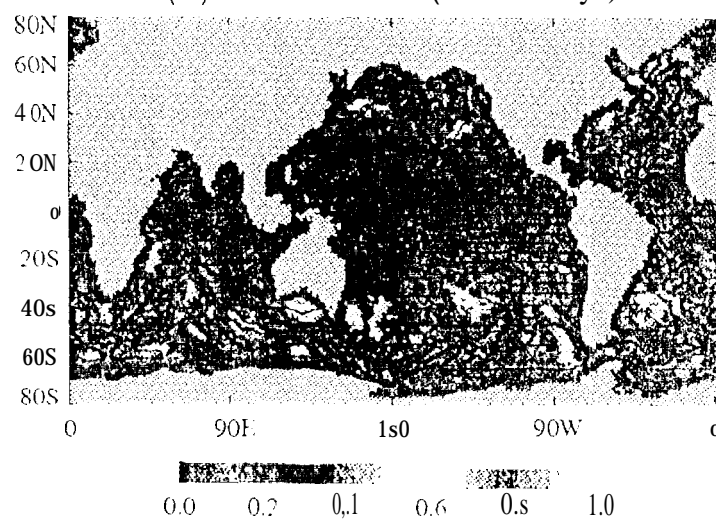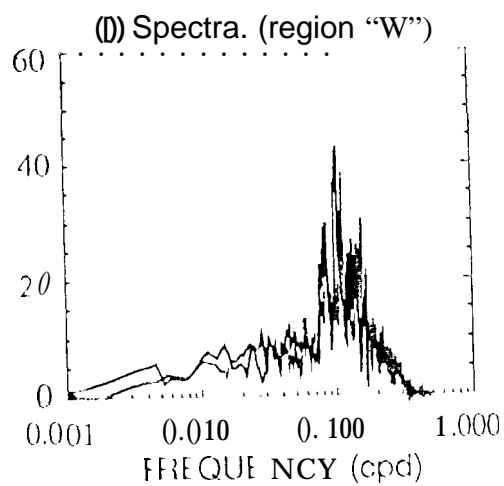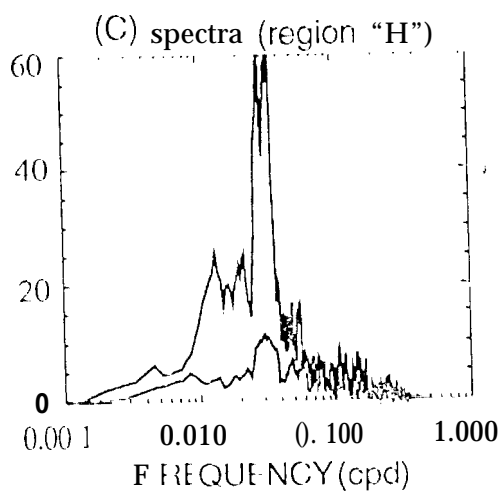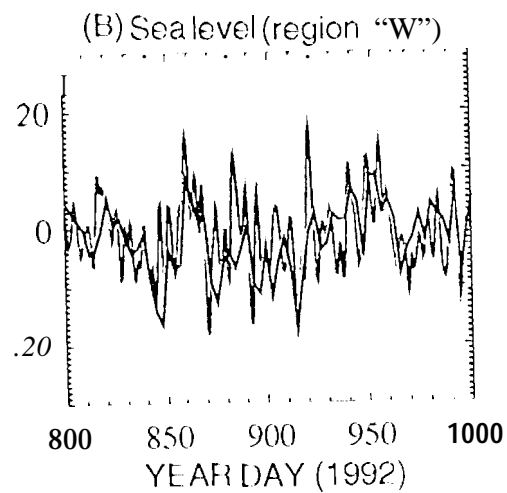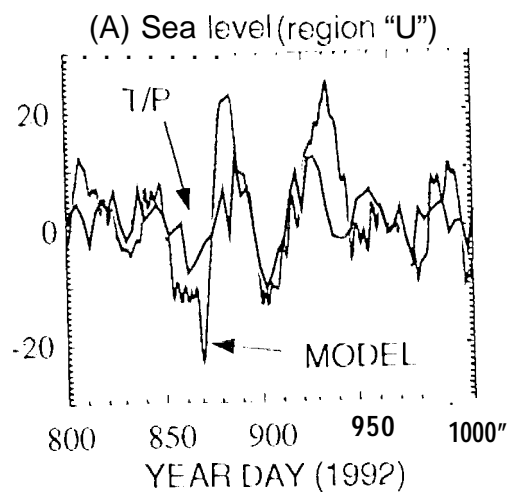
(A) Coherence   (B) F'base

(A) Coherence

(El) Phase
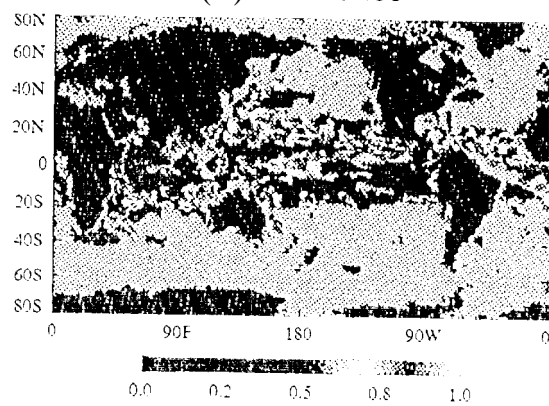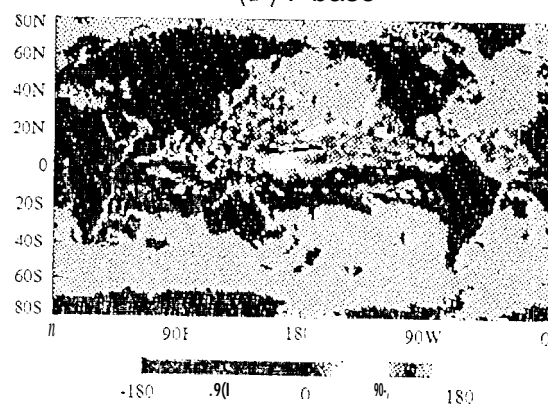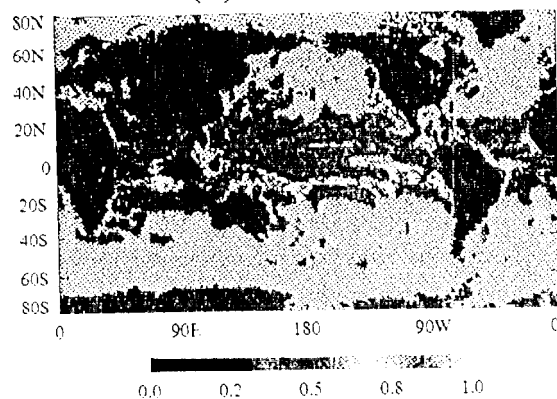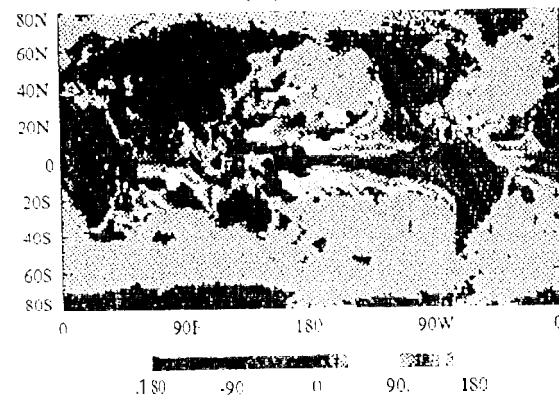
(A) Total APE
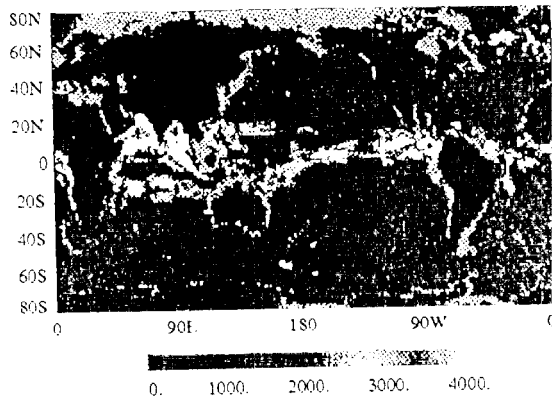
(B) First baroclinic mode
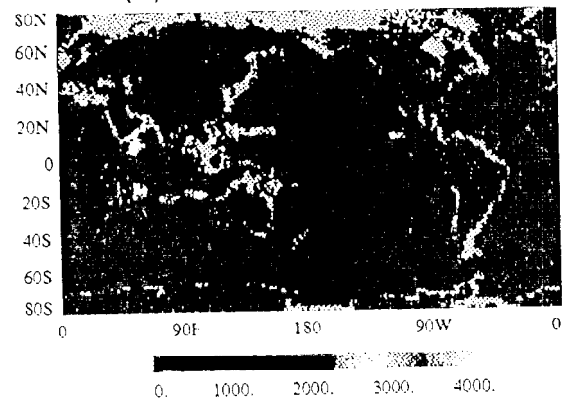
(C) Second baroclinic mode
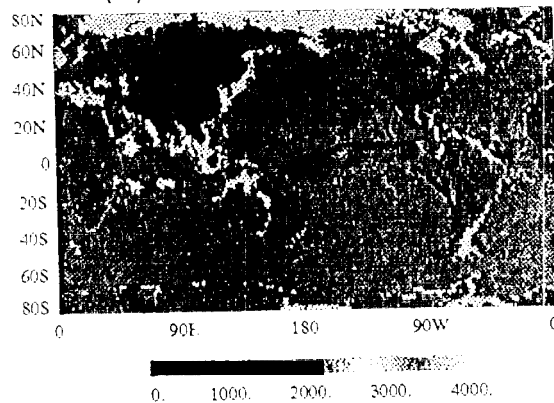
(D) % of APE- in first baroclinic mode
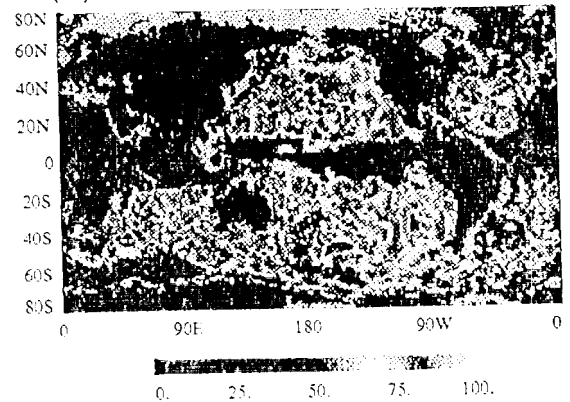
(A) KE of barotropic mode
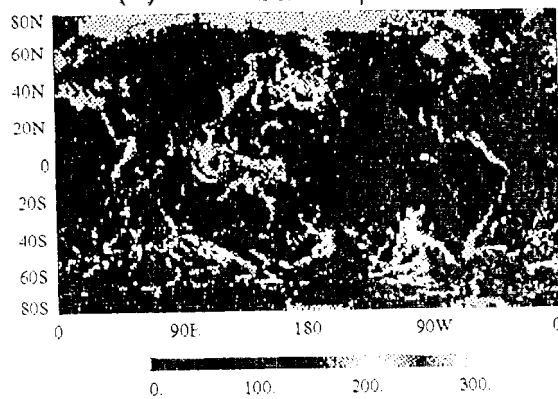
(B) First baroclinic mode
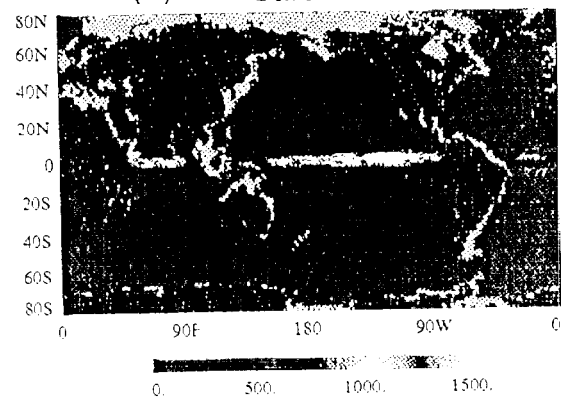
(C) Second baroclinic mode
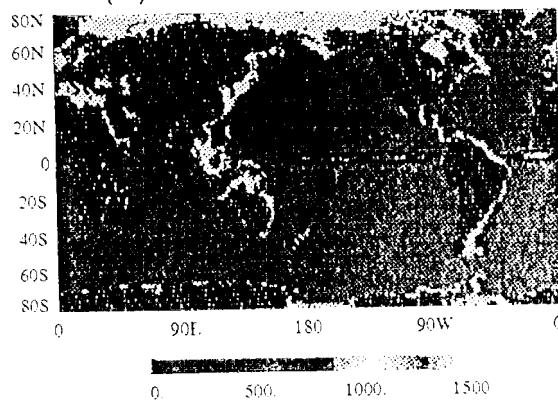
(D) % of KE in barotropic mode

(A) Total variability

(B) Variability without trend

(C) Trend

(D) Trend with alternate forcing

80

40

LATITUDE (°N)

0

40

80

0.001   0.01   0.1   1.0

FREQUENCY (cpd)

3

(A) Diego Garcia

TIDE GAUGE

MODEDEL

Frequency (cpd)

(B) Kerguelen

Frequency (cpd)

5

Figure showing explained sea level variance (cm²) versus Year Day (1992), with curves labeled "with 12h window" and "with 3-day window".
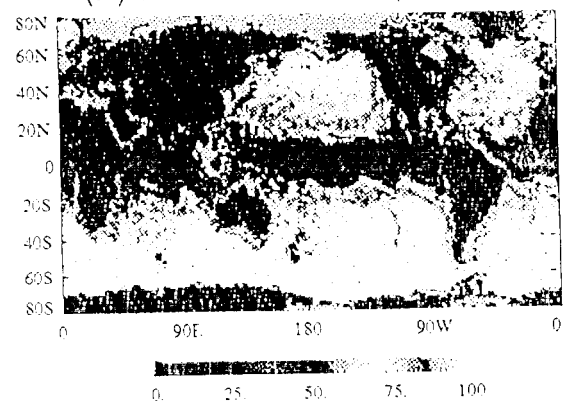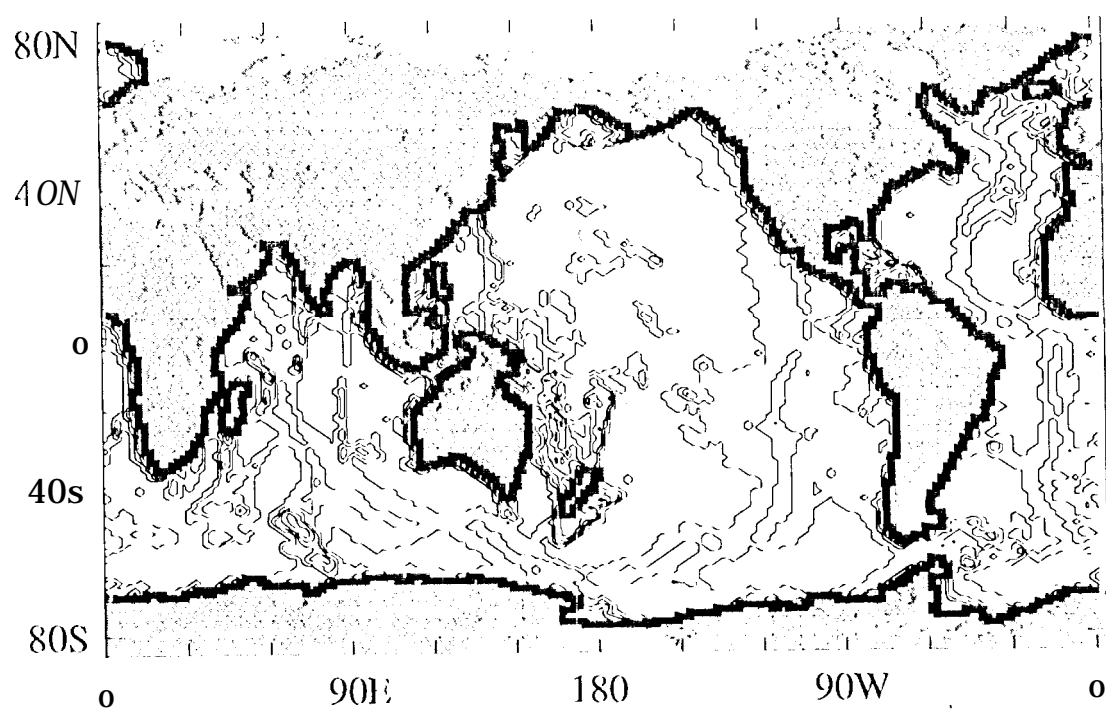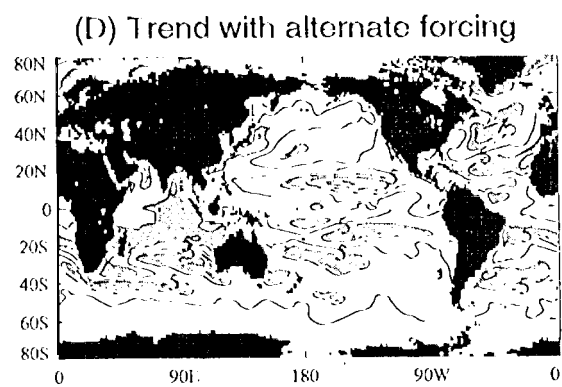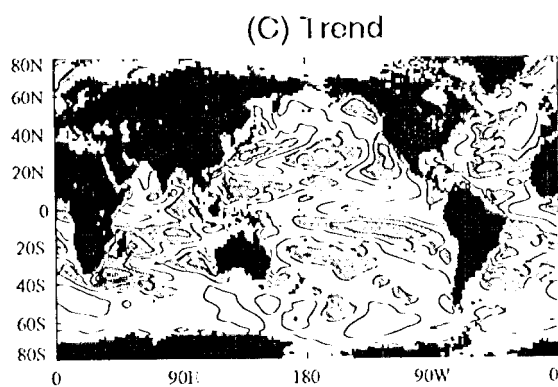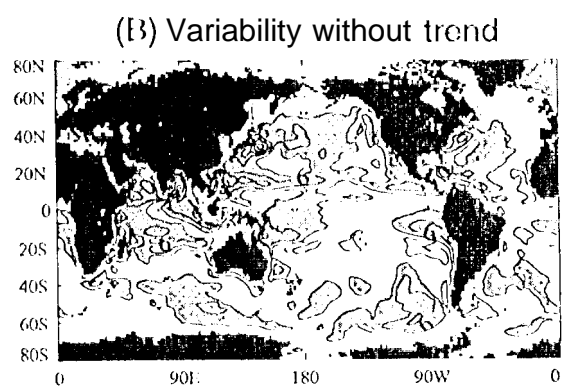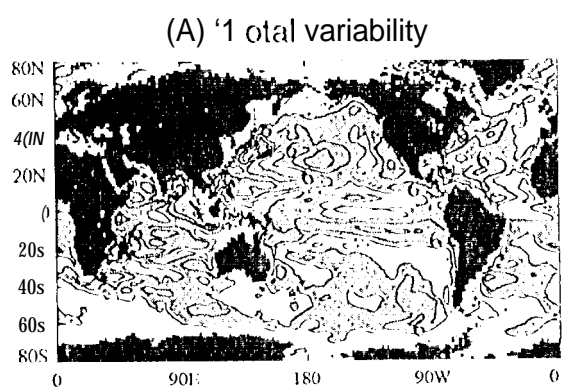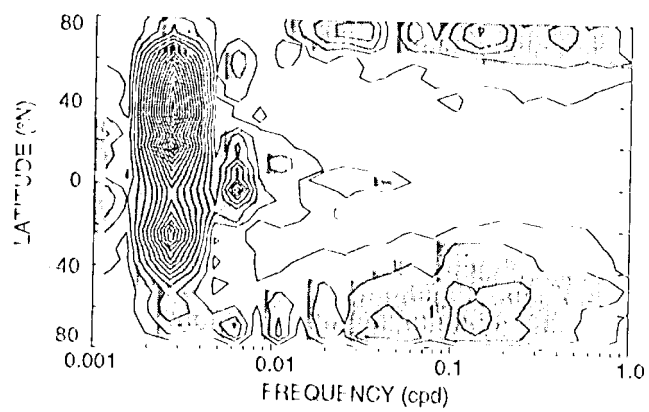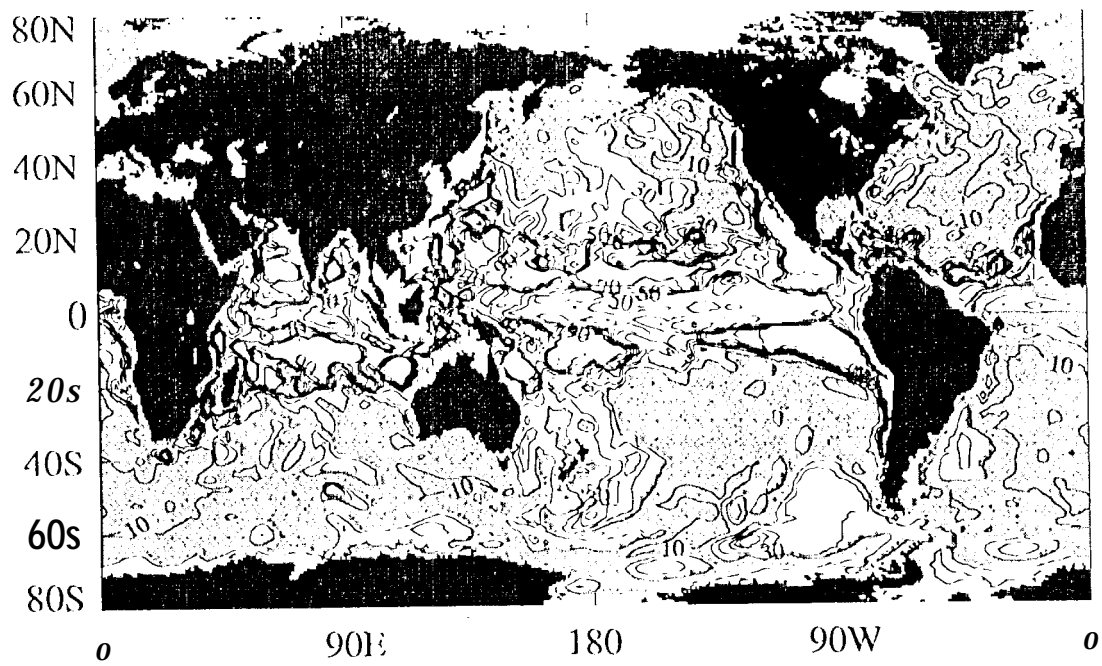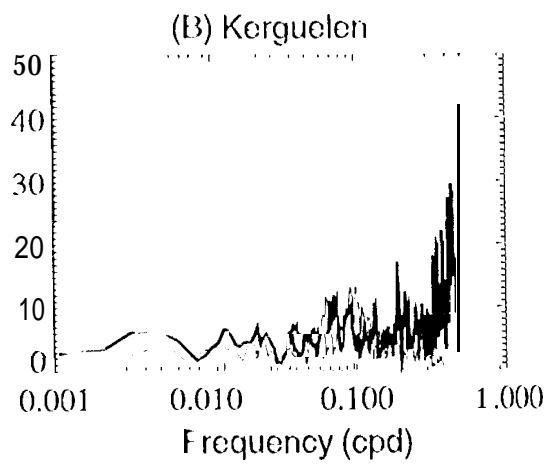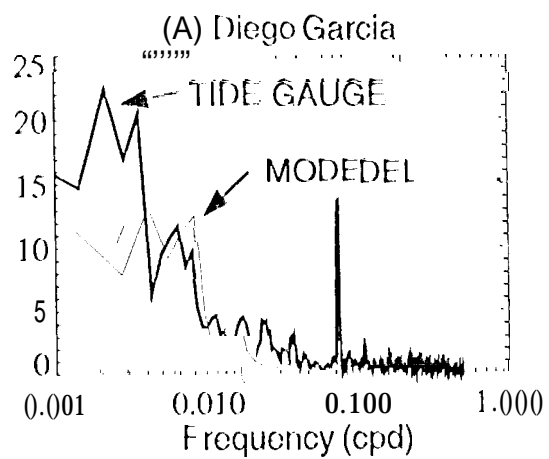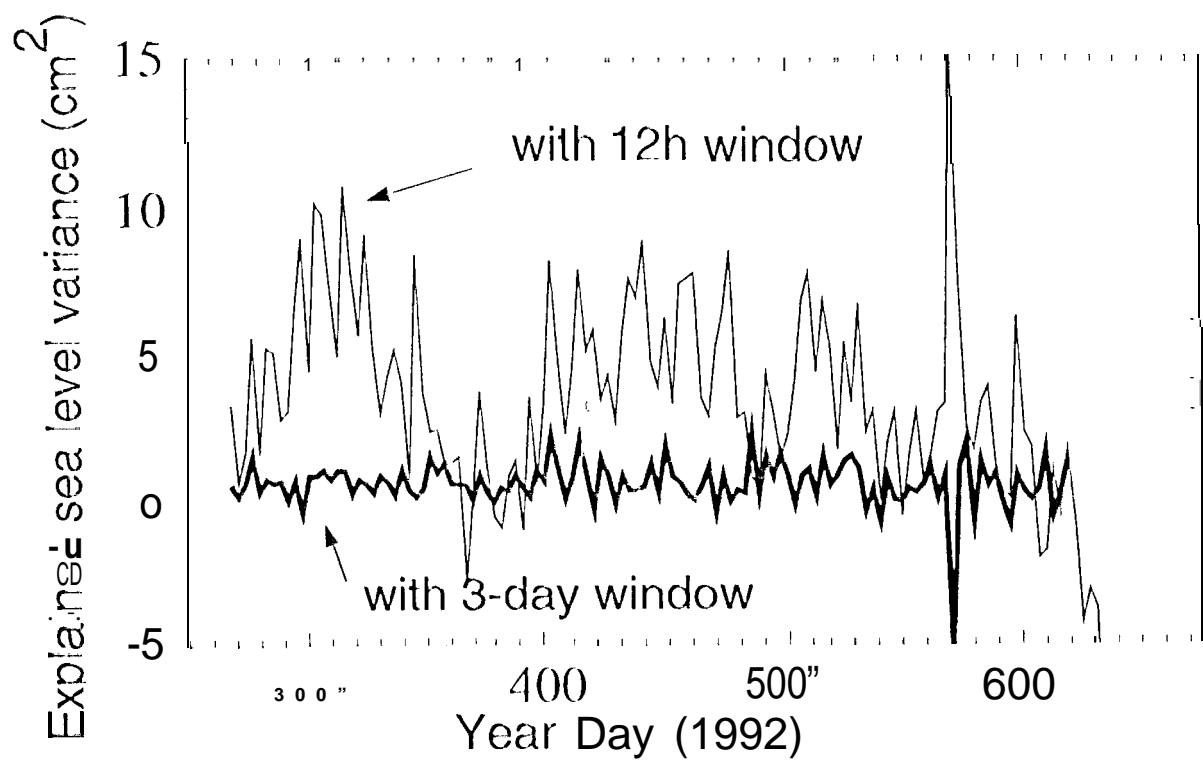
(A) Effects of heating/cooling
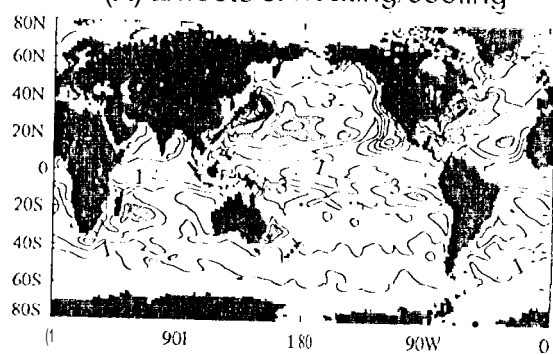
(B) Effects of winds
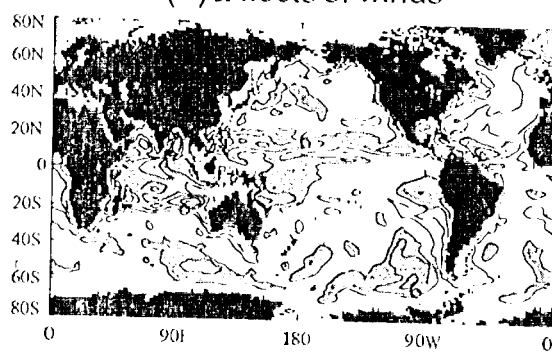
(C) Percentage due to heating/cooling
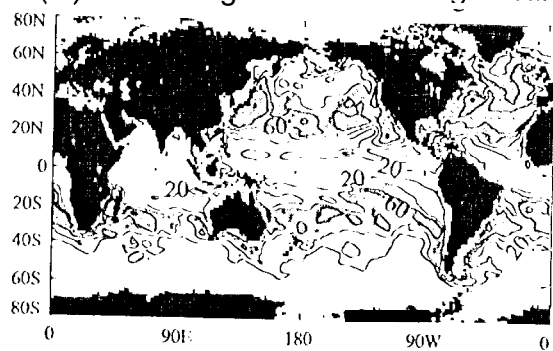
(A) Short wave radiation
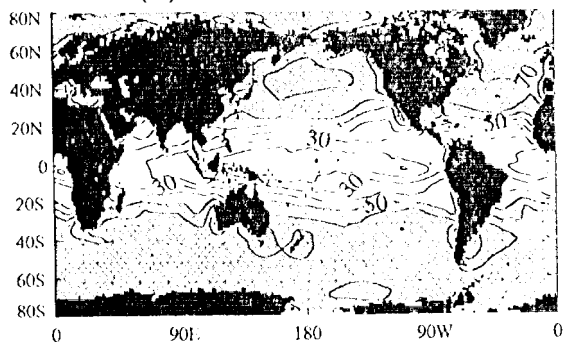
(B) Latent heat flux
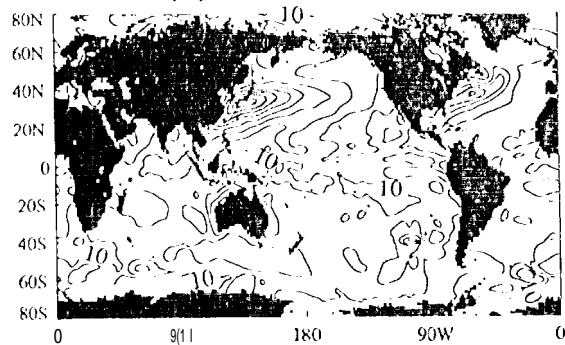
(C) Long wave radiation
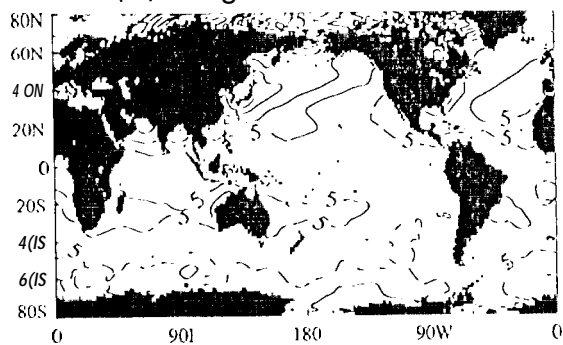
(D) Sensible heat flux
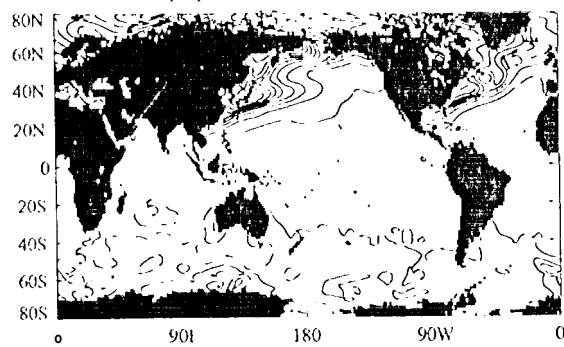
(E) Net heat flux
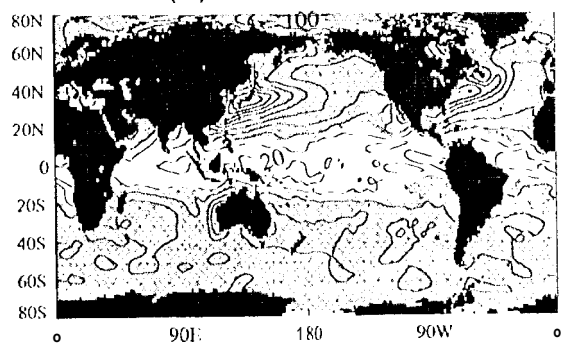
(A) Thermal expansion coefficient

(B) heat flux induced sea level change

(A) Frequency Spectra

(B) % at annual period

10

(A) Barotropic
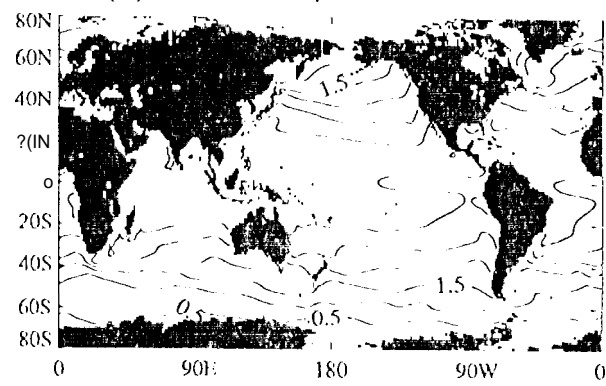
(B) Baroclinic

(C) % by baroclinic
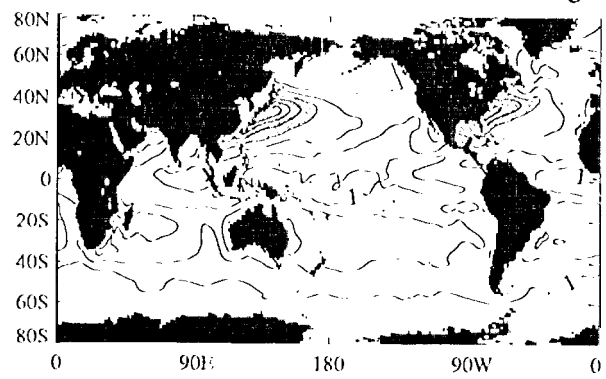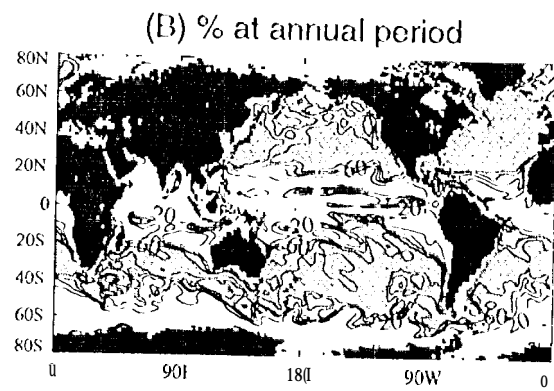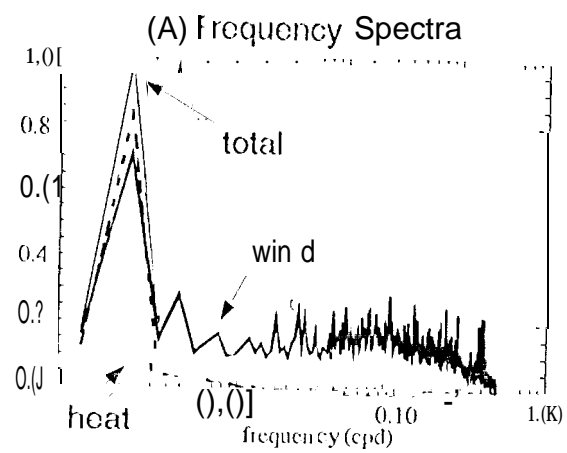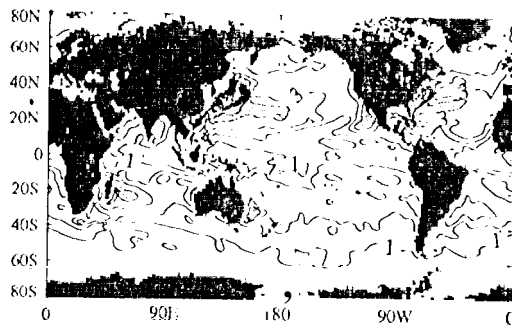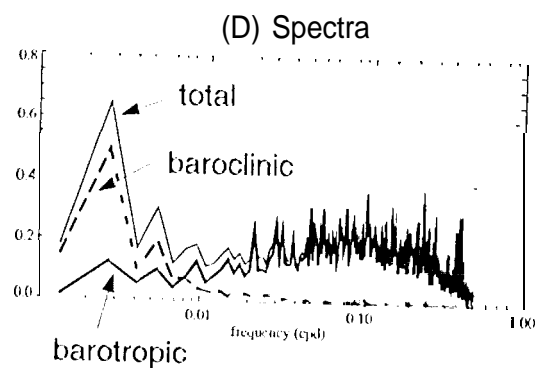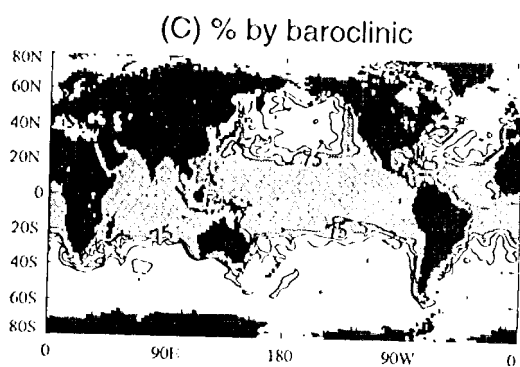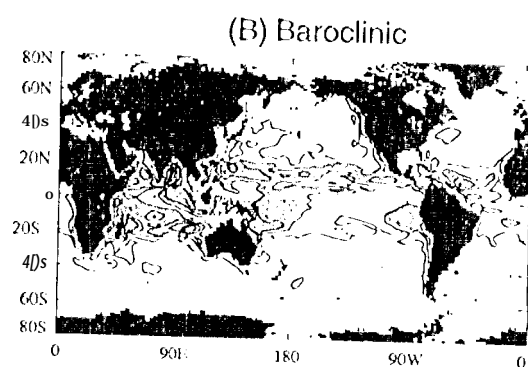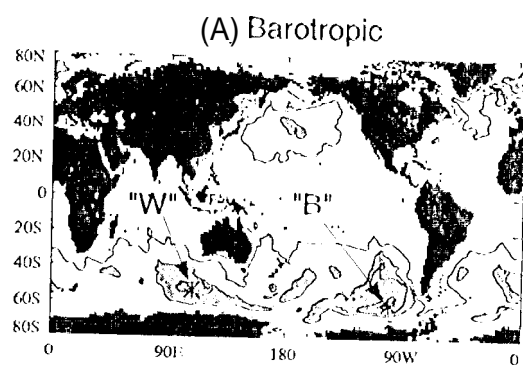
(D) Spectra

(A) Variance of wind stress curl

(B) Spectra

0° - 20°N

60°S - 40°S

frequency (cpd)

(A) First baroclinic Rossby wave

(B) Barotropic Rossby wave

(C) Wind forcing for (A)

(D) Wind forcing for (B)

14

(A) Sea level

(100°W, 60°S)

(108"[-, 53"s))

f '

(B) Wind stress curl

15
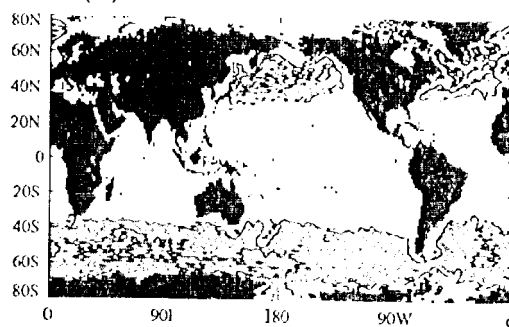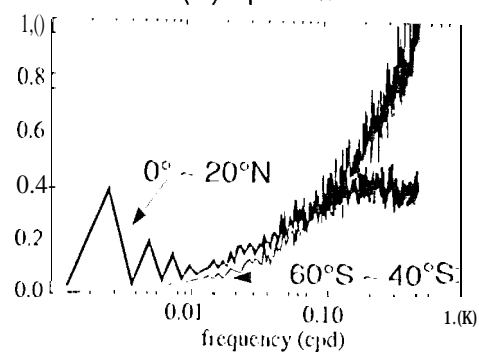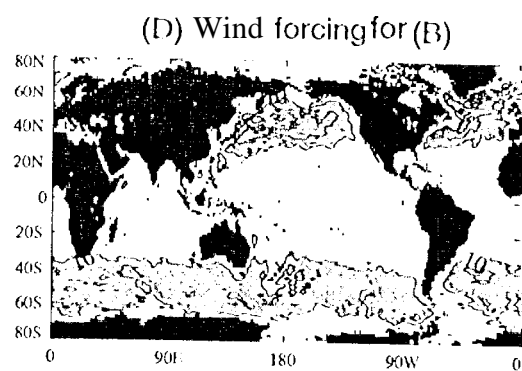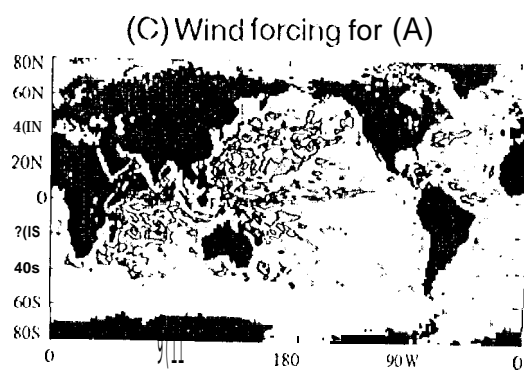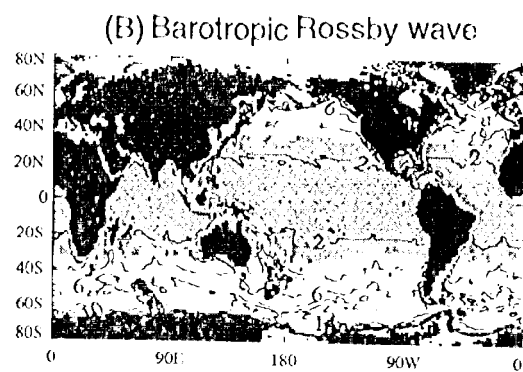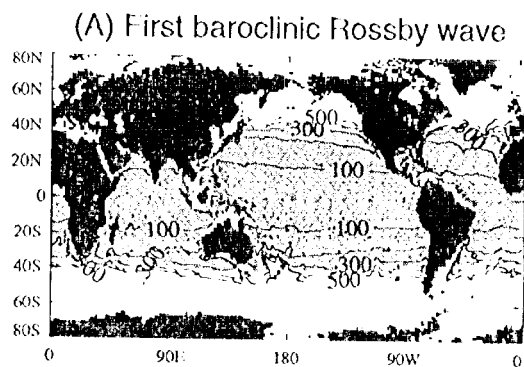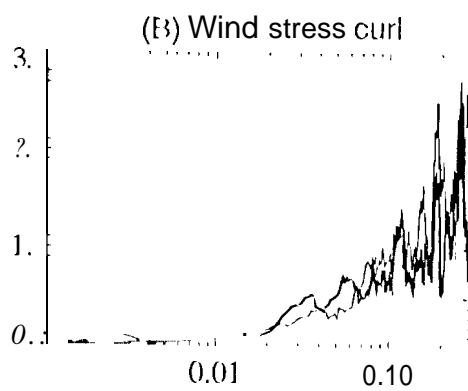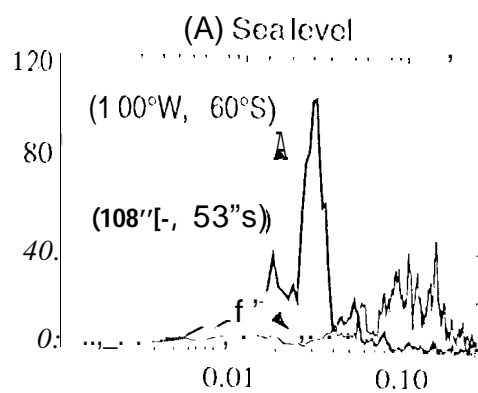
(A) Annual

([3) 10 to 100 days

16

(A) First bariclinic mode

(PI) Second baroclinic mode

(C) Ratio of @) to (A)

17
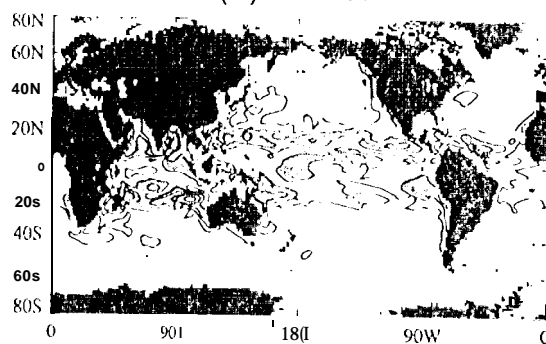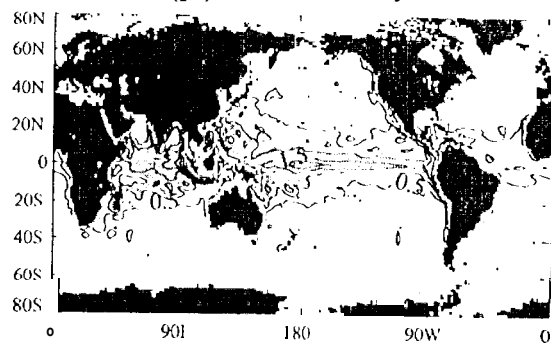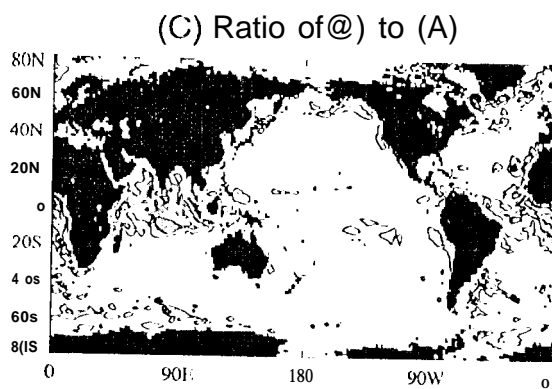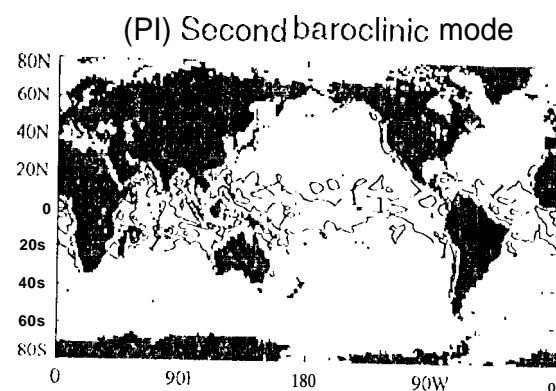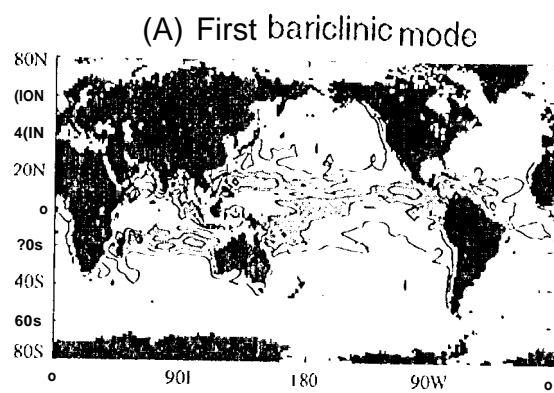
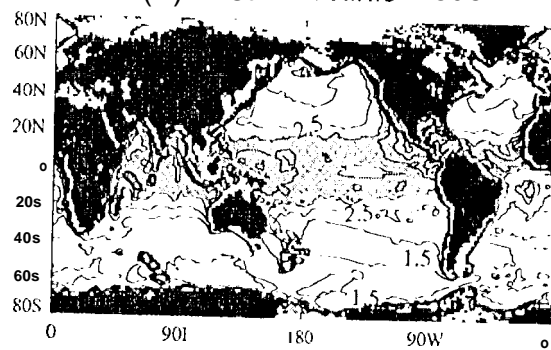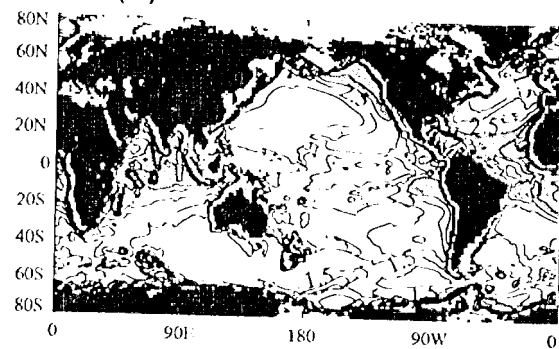## (A) First baroclinic mode

(B) Second baroclinic mock

(C) Ratio of (B) to (A)